Quantum fluid dynamics in the Lagrangian representation and applications to photodissociation problems

Fernando Sales MayorAttila AskarHerschel A. Rabitz

Citation: The Journal of Chemical Physics **111**, 2423 (1999); doi: 10.1063/1.479520
View online: http://dx.doi.org/10.1063/1.479520
View Table of Contents: http://aip.scitation.org/toc/jcp/111/6
Published by the American Institute of Physics



Quantum fluid dynamics in the Lagrangian representation and applications to photodissociation problems

Fernando Sales Mayor[a)]
Koç University, Mathematics Department, Istinye, 80860 Istanbul, Turkey
and Princeton University, Chemistry Department, Princeton, New Jersey 08540

Attila Askar
Koç University, Mathematics Department, Istinye, 80860 Istanbul, Turkey

Herschel A. Rabitz
Princeton University, Chemistry Department, Princeton, New Jersey 08540

(Received 31 August 1998; accepted 23 February 1999)

This paper considers the practical utility of quantum fluid dynamics (QFD) whereby the time-dependent Schrödinger's equation is transformed to observing the dynamics of an equivalent ''gas continuum.'' The density and velocity of this equivalent gas continuum are respectively the probability density and the gradient of the phase of the wave function. The numerical implementation of the QFD equations is carried out within the Lagrangian approach, which transforms the solution of Schrödinger's equation into following the trajectories of a set of mass points, i.e., subparticles, obtained by discretization of the continuum equations. The quantum dynamics of the subparticles which arise in the present formalism through numerical discretization are coupled by the density and the quantum potential. Numerical illustrations are performed for photodissociation of NOCl and NO_2 treated as two-dimensional models. The dissociation cross sections $\sigma(\omega)$ are evaluated in the dramatically short CPU times of 33 s for NOCl and 40 s for NO_2 on a Pentium-200 MHz PC machine. The computational efficiency comes from a combination of (a) the QFD representation dealing with the near monotonic amplitude and phase as dependent variables, (b) the Lagrangian description concentrating the computation effort at all times into regions of highest probability as an optimal adaptive grid, and (c) the use of an explicit time integrator whereby the computational effort grows only linearly with the number of discrete points.
© *1999 American Institute of Physics.* [S0021-9606(99)02019-X]

I. INTRODUCTION

The conventional approach for describing quantum mechanics is via Schrödinger's equation, but an alternative equivalent formalism is quantum fluid dynamics (QFD).[1–3] In this representation, quantum mechanics is described in terms of a density and a velocity field which jointly obey the usual mass and momentum conservation equation of hydrodynamics for a compressible fluid with a particular constitutive law.[4,5] The essence of the formalism is the polar representation of the complex wave function ψ by its amplitude A and phase S as $\psi = A \exp(iS/\hbar)$, as opposed to the Cartesian representation by its real and imaginary parts as $\psi = \psi_R + i\psi_I$. This formalism was derived originally by Madelung in 1926,[6] elaborated on by de Broglie in his work spanning the period 1927–1967 (Ref. 7) and further expanded starting in the 1950s by Bohm[8] and others.[9,10]

The QFD formulation requires solving a set of nonlinear partial differential equations. In this sense, QFD may be seen as a step in the wrong direction as compared to the linear Schrödinger equation. However, within QFD, the oscillatory real and imaginary components of the complex wave function are replaced by the near monotonous amplitude and phase. This aspect of QFD can be illustrated in the simplest context with the plane wave $\psi = \exp i(kx - \omega t)$. The real and imaginary parts of ψ are the oscillatory cosine and sine functions, while its amplitude is a constant and its phase is linear in both the time and space coordinates. This behavior may be exploited as a significant computational advantage by regarding the amplitude and the phase as the unknown fields to be discretized. In this spirit, the QFD formalism has been utilized to generate numerical algorithms for solving time-dependent scattering problems[11–15] and many electron systems.[16–23] The nonlinear field equations of QFD have also been suggested as a natural framework for studying fundamentally nonlinear phenomena such as solitons[20] and chaos.[24]

Classical fluid dynamics can be described in terms of the equivalent Eulerian and Lagrangian representations. In the former case, the dynamics is observed by ''monitors'' that are fixed in space, while in the latter method, the monitors ride with the fluid particles. Consequently, in the Eulerian method, the calculations are carried out by reference to a fixed coordinate system; in the Lagrangian method, trajectories of the fluid mass points are followed. The work in Refs. 16–23 utilizes the Eulerian representation with an implicit numerical integration method, while the work in Refs. 11–13

[a)]On leave from Instituto de Matematicas y Fisica Fundamental (C.S.I.C.), Serrano 123, 28006 Madrid, Spain.

 © 1999 American Institute of Physics

is based on the numerical implementation of the Lagrangian representation with an explicit time integration scheme. The numerical implementation of the Lagrangian scheme produces an optimal adaptive grid at all times as a result of following the particles that are placed in regions of highest probability density.

The QFD formalism replaces the evolving wave function and operator representations by an ensemble of mass points in classically familiar terms, although fully quantum mechanical, for a more intuitive interpretation of the dynamics. There has been similar efforts for visualizing quantum phenomena in terms of graphical representations of the flows and wave structures in scattering theory.[25,26] Finally, several wave packet calculations,[27,28] semiclassical methods,[29] the WKBJ method for both the Schrödinger and Dirac equations,[30] and discrete variable representation (DVR) scheme[31] as well as general integration schemes of the time-dependent Schrödinger equation[32,33] share features resembling those addressed in the present formulation.

A wealth of computational algorithms exist for solving the Navier–Stokes equations describing classical fluid dynamics that can be beneficial for the numerics involved in the QFD formulation.[34–39] QFD, for many particles systems, has the expected difficulties associated with higher dimensions, as compared to classical fluid dynamics problems defined by up to three space coordinates. In the case of multiparticle QFD, the ''alternating direction'' methods offers an attractive solution procedure where the n-dimensional space is reduced to a set of n one-dimensional problems at each time step.[40,41] The alternating direction scheme is applied in another paper to multidimensional quantum mechanical problems treated by QFD.[42] Particular challenges for Lagrangian fluid dynamics includes the design of a suitable representation method over irregular meshes in higher dimensions and the treatment of the boundary points. In this regard, the reproducing kernel Hilbert space (RKHS) method appears as a promising avenue in view of its proven success for representing multivariate functions with sparse irregular grids.[43–46]

This paper implements the QFD formalism within the Lagrangian representation. The spirit of the formulation is to be found in an earlier work.[12] The extensions here are both formal and in terms of numerical implementation. The finite elements methodology is utilized for the space discretization over the irregular grids formed by the motion of the fluid particles in the Lagrangian dynamics. The time integration is performed with an explicit scheme.[47] Applications of the formulation are presented for the photodissociation[48–57] for NOCl and NO_2, treated as model two-dimensional systems. The organization of the paper is as follows. Section II presents the basic formulation for QFD. The essential steps leading to the discretization of the field equations are presented in Sec. III. The formulation is applied in Sec. IV to the photodissociation of NOCl and NO_2. A discussion on the methodology and the specific results are presented in Sec. V. The technical details relating to the numerical algorithm and the specifics of the potential surfaces involved along with the evaluation of the initial wave packet are presented in the Appendices.

II. QFD FORMULATION

The starting point of the derivation is the Schrödinger equation

$$i\hbar\psi_t = -(\hbar^2/2m)\nabla^2\psi + V\psi. \tag{2.1}$$

Subscripts will be used to indicate partial derivatives (e.g., $\psi_t = \partial\psi/\partial t$). Substitution of the complex wave function ψ in polar form as

$$\psi(\mathbf{x},t) = A(\mathbf{x},t)\exp[iS(\mathbf{x},t)/\hbar] \tag{2.2}$$

into the Schrödinger equation in Eq. (2.1), and the separation of its imaginary and real parts followed by a minor rearrangement yields

$$\rho_t + \nabla\cdot(\rho\mathbf{v}) = 0, \tag{2.3}$$

$$S_t + 1/2m|\mathbf{v}|^2 + V + V_{qu} = 0, \tag{2.4}$$

where

$$\rho = A^2,$$

$$\mathbf{v} = \nabla S/m, \tag{2.5}$$

$$V_{qu} = -(\hbar^2/2m)\nabla^2 A/A = -(\hbar^2/2m)(\nabla^2 \log A + |\nabla \log A|^2).$$

The second form for V_{qu} is numerically advantageous as $\log A$ is a more slowly varying function than A. Equation (2.3) is identified as the conventional mass conservation law equation of fluid dynamics for a compressible gas with the density $\rho(\mathbf{x},t)$ and velocity field $\mathbf{v}(\mathbf{x},t)$. The phase $S(\mathbf{x},t)$ is seen to play the role of a velocity potential for $\mathbf{v}$ (Refs. 4,5) in view of the definition in Eq. (2.5). Equation (2.4) is interpreted as an energy conservation law: $\frac{1}{2}m|\mathbf{v}|^2 + V$, forms the classical energy with the usual kinetic and potential energy components; V_{qu} is a nonlocal ''quantum potential'' as the Laplacian connects neighboring regions; S is an action whose time rate S_t is an energy.

A momentum conservation equation can be derived by taking the gradient of the energy expression in Eq. (2.4). The use of the vector identity $\nabla(\mathbf{a}\cdot\mathbf{b}) = \mathbf{a}\cdot\nabla\mathbf{b} + \mathbf{b}\cdot\nabla\mathbf{a} + (\nabla\times\mathbf{a})\times\mathbf{b} + (\nabla\times\mathbf{b})\times\mathbf{a}$ with $\mathbf{a} = \mathbf{b} = \nabla A$ permits a rearrangement of this equation as

$$m(\mathbf{v}_t + \mathbf{v}\cdot\nabla\mathbf{v}) = -\nabla(V + V_{qu}). \tag{2.6}$$

The term $\mathbf{v}_t + \mathbf{v}\cdot\nabla\mathbf{v}$ is the acceleration in fluid dynamics composed of the local acceleration $\mathbf{v}_t$ and the convected component $\mathbf{v}\cdot\nabla\mathbf{v}$.[4,5,12] As the momentum and energy conservation equations are equivalent, the dynamics can alternatively be defined by the mass and energy conservation [i.e., through the set of equations in (2.3) and (2.4)], or through the mass and momentum conservation equations [i.e., through the set of equations in (2.3) and (2.6)]. The calculations of this paper utilize the mass and momentum conservation equations.

The above description of the dynamics of a fluid continuum with respect to a fixed coordinate system is referred to as the ''Eulerian'' representation.[4,5] In the Eulerian description of classical fluids, the dynamics of the fluid continuum is observed by placing ''monitors'' at the sites of a fixed grid in space. The observers record the density $\rho(\mathbf{x},t)$, the velocity $\mathbf{v}(\mathbf{x},t)$ and other fields such as the pressure, ve-

locity potential and determine the stream lines when needed. In contrast, the ''Lagrangian'' method corresponds to the description of the hydrodynamics where monitors ''ride'' with the fluid particles. In this case, the observers must also record the location of the particles they ride with as a function of time in addition to the fields in the Eulerian description. In the Lagrangian description, the identity of a fluid particle is marked by its initial position and this identity is kept throughout the process.[4,5,12]

The Lagrangian representation is obtained by rewriting Eqs. (2.3)–(2.6) of the Eulerian representation in the convected coordinates.[4,5,12] This reduces to following the time evolution of a typical function $f(\mathbf{x},t)$ (e.g., the fields ρ, S, and $\mathbf{v}$) at a point $\mathbf{x}$ with the trajectory $\mathbf{x}=\mathbf{x}(t)$ such that $f(t)=f(\mathbf{x}(t),t)$. The total time derivative of $f(\mathbf{x},t)$ is indicated by a dot and is evaluated by the chain rule as

$$\dot{f}=df/dt=\partial f/\partial t+(d\mathbf{x}/dt)\cdot\nabla f=f_t+\mathbf{v}\cdot\nabla f. \tag{2.7}$$

In obtaining the above expression, the position vector $\mathbf{x}$ of a particle is related to the velocity $\mathbf{v}$ in the usual way as

$$\dot{\mathbf{x}}=\mathbf{v}. \tag{2.8}$$

The time history of a particle as $\mathbf{x}(t)$ defines a trajectory in configuration space in a manner analogous to classical dynamics in view of its time derivative being identified as the velocity $\mathbf{v}$.

The mass and momentum conservation laws above become

$$\dot{\rho}+\rho\nabla\cdot\mathbf{v}=0, \tag{2.9}$$

$$m\dot{\mathbf{v}}=\mathbf{F}, \tag{2.10}$$

where

$$\mathbf{F}=-\nabla(V+V_{qu}). \tag{2.11}$$

Equations (2.9) and (2.10) along with the definition of velocity $\mathbf{v}$ and force $\mathbf{F}$, respectively, in Eqs. (2.8) and (2.11) form a complete set to determine the trajectory of the fluid particles. Equation (2.10) yields the following interpretation of the momentum equation within the Lagrangian formalism: the evolution of the wave function described by the Schrödinger equation in (2.1) is equivalent to following the ensemble of trajectories of a continuum of particles of mass m subjected to the force $\mathbf{F}$ derived from the total potential made of the sum of classical and quantum components V and V_{qu} as given in Eq. (2.4). There is, however, a fundamental difference with classical trajectory calculations where the particles are ''real'' entities and each trajectory is independent. For QFD, the ''quantum subparticles'' (i.e., the particles of the fluid continuum) only collectively represent the physical particles, and their dynamics are coupled through the continuity equation and the quantum potential.

III. NUMERICAL ANALYSIS

The main ideas involved here are for the Lagrangian description and the details of the derivations are carried out in two-dimensions in Appendix A. The extensions of the derivations to arbitrary dimensions and multiple particles are conceptually straightforward. A general multidimensional treatment within the Eulerian description is presented in Ref. 42.

A. Space discretization

A set of discrete nodes within the continuum is identified by the coordinates $\{\mathbf{x}_i\}$. In the Lagrangian representation, the nodes move such that $\mathbf{x}_i=\mathbf{x}_i(t)$. The various fields are discretized at these nodes as

$$f_i=f_i(t)=f(\mathbf{x}_i(t),(t)). \tag{3.1}$$

Following the localization rule in Eq. (3.1), the discretized forms of the basic conservation laws in Eqs. (2.9) and (2.10) and the definition in Eq. (2.8) read

$$\begin{aligned}&\dot{\rho}_i+\rho_i(\nabla\cdot\mathbf{v})_i=0,\\ &m\dot{\mathbf{v}}_i=\mathbf{F}_i(t),\\ &\dot{\mathbf{x}}_i=\mathbf{v}_i,\end{aligned} \tag{3.2}$$

where, following the definition in Eq. (2.11),

$$\begin{aligned}&\mathbf{F}_i=-[\nabla(V+V_{qu})]_i,\\ &(V_{qu})_i=-(\hbar^2/2m)(\nabla^2\log A+|\nabla\log A|^2)_i.\end{aligned} \tag{3.3}$$

The set of equations above transform the solution of Schrödinger's equation into following the trajectories $\{\mathbf{x}_i(t)\}$ for the set of interacting mass points labeled by the indices i. The dynamics of the particles are coupled through the density and the quantum potential. The trajectory equations can be integrated without the need of the phase in terms of its gradient which is the velocity. When needed, the phase is calculated from the discretized energy conservation law in Eq. (2.4) as

$$\dot{S}_i=1/2m\mathbf{v}_i\cdot\mathbf{v}_i-(V+V_{qu})_i. \tag{3.4}$$

This equation is used for calculating the dissociation cross section as in the applications in the next section.

B. Spatial derivatives

The partial derivatives $\nabla\cdot\mathbf{v}$, $\nabla^2\log A$ and $\nabla\log A$ appear in the basic conservation laws in Eqs. (3.2) and (3.3). This problem reduces to deriving the numerical differentiation formulas for f_x, f_y for a typical function $f(x,y)$ over an irregular grid. The divergence of a vector function $\mathbf{u}=(u,v)$ is obtained by the use of the general derivative formulas in the x and y components as required by the definition $\nabla\cdot\mathbf{u}=u_x+v_y$. Similarly, the Laplacian $\nabla^2 f=f_{xx}+f_{yy}$ is evaluated by using the first order derivative formulas twice as indicated. The basic partial differentiation formulas are obtained by constructing the cells defined by the discrete nodes and using suitable interpolations over these local regions. Figure 1 shows a typical cell as an irregular polygon defined by eight corners and an interior point. Within the Lagrangian formalism of moving grid points, the cells are ever deforming irregular shapes. The present formulation takes advantage of finite element techniques[26,58–62] that map the irregular cells onto a square in an auxiliary space. In this second space with the simple geometry for the cells, straightforward local interpolation approximations permit the nu-

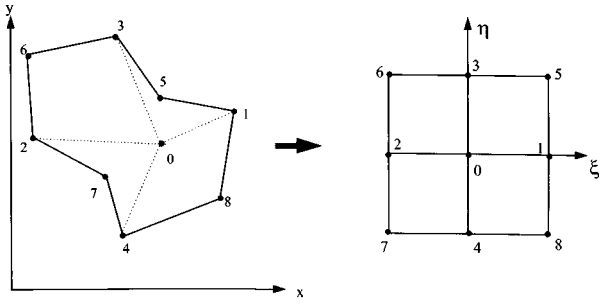


FIG. 1. The mapping of an irregular nine point finite element in the (x,y) plane onto a square in the (ξ,η) plane.

merical evaluation of the derivatives. The technical aspects of the formalisms are well established.[59,60] Appendix A presents the derivations and the specific expressions for the polygonal region in Fig. 1 that are used in the calculations of the next section.

C. Time integration

The explicit centered difference scheme[43] is adopted for time integration. Within the complex wave form, this scheme has been shown to be stable under the condition $(\hbar/2m)\,\Delta t/\Delta x^2<1$, where Δt and Δx indicate the discrete time step and a measure of the mesh size. For the practical aspects of the stability with the Lagrangian formulation, the distance $v\Delta t$ traveled by the particles with velocity v during the time span of Δt should be less than the cell dimensions leading to the additional criterion of stability as $v\Delta t/\Delta x<1$. This condition preserves the connectivity of the nodes in the sense that a point inside or outside a polygonal region formed by its neighbors at the initial time remains so throughout the dynamics, as the cells deform.

The mass conservation law in Eq. (3.2) is of a special structure that can be integrated exactly for the density $\rho_i=\rho(\mathbf{x}_i,t)$ at the point $\mathbf{x}_i$ between the general time steps t_1 and t_2,[12] as $\rho_i(t_2)=\rho_i(t_1)\exp\{-\int_{t_1}^{t_2}[\nabla\cdot\mathbf{v}(t)]_i dt\}$. With $t_1=t-\Delta t$ to $t_2=t+\Delta t$ and using the explicit centered difference approach for $\int_{t-\Delta t}^{t+\Delta t}[\nabla\cdot\mathbf{v}(t)]_i dt$ as $2\Delta t[\nabla\cdot\mathbf{v}(t)]_i$, the integration of the discretized mass conservation equation becomes

$$\rho_i(t+\Delta t)=\rho_i(t-\Delta t)\exp[-2\Delta t(\nabla\cdot\mathbf{v}(t))_i]. \tag{3.5}$$

The space discretized version of the momentum conservation law in Eq. (3.2) is similarly integrated within the centered difference scheme between the times $t-\Delta t$ and $t+\Delta t$ to obtain

$$\mathbf{v}_i(t+\Delta t)=v_i(t-\Delta t)+2\Delta t\mathbf{F}_i(t). \tag{3.6}$$

The particle positions are likewise evaluated from the velocities according to Eq. (3.2) as

$$\mathbf{x}_i(t+\Delta t)=\mathbf{x}_i(t-\Delta t)+2\Delta t\mathbf{v}_i(t). \tag{3.7}$$

The formulation here in terms of the density ρ and velocity $\mathbf{v}$ bypasses the need to calculate S. When needed, as in the calculation of the dissociation cross section in Sec. IV, S is evaluated from Eq. (3.4) at each time step, again in the explicit centered difference approach, as

$$S_i(t+\Delta t)=S_i(t-\Delta t)+2\Delta t[\tfrac{1}{2}m\mathbf{v}_i(t)\cdot\mathbf{v}_i(t) -(V(t)+V_{qu}(t))_i]. \tag{3.8}$$

The alternative of calculating S from the velocity field $\mathbf{v}=\nabla S/m$ according to Eq. (2.4) is not carried as this would necessitate an additional numerical integration.

IV. APPLICATIONS TO PHOTODISSOCIATION

The time-dependent study of photodissociation is defined by two potential energy surfaces S_0 and S_1 corresponding, respectively, to the electronic ground and excited states of the system. The S_0 surface typically has a pronounced well leading to the presence of bound states. The S_1 surface on the other hand, may have shallow wells sustaining only a weakly bound state; or as seen in Figs. 2 and 3 for NO_2,[49] the shallow wells may not be able to support bound states. Similarly, the S_1 surface may not even have an equilibrium point as seen in Fig. 4 for the case of NOCl.[48] The S_0 surface is used for determining the molecular bound state which provides the initial wave function. The dynamical part of the problem consists of following the evolution of this initial bound state on the S_1 surface. The initial wave created on S_0 is raised onto the S_1 surface by the optical field within the Franck–Condon approximation.

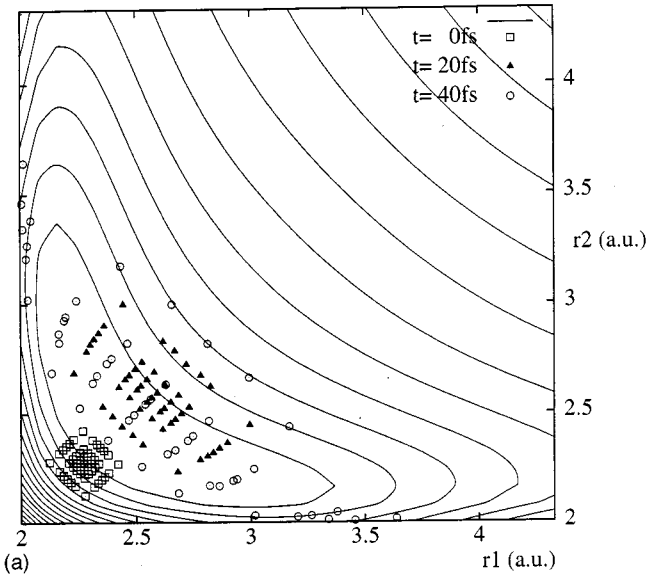
Dissociation in the present context is defined by the wave function spreading indefinitely and moving away from the region where it is initially localized about the equilibrium point. The QFD Lagrangian formalism is most suitable for visualizing the ''flow'' as displayed in Figs. 2–4. Quantitatively, the dissociation at the pump energy ω is described by the cross section $\sigma(\omega)$ (Refs. 48,49) evaluated through

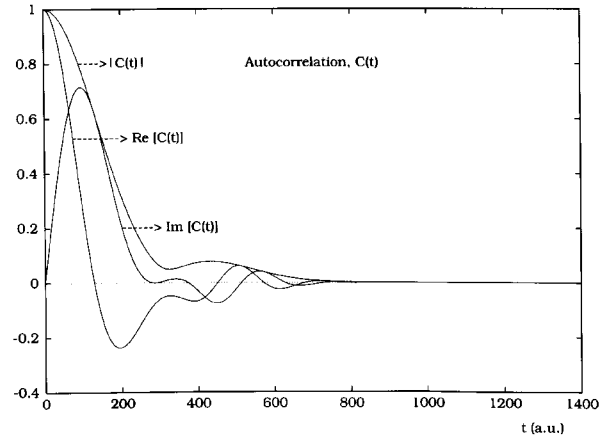
$$C(t)=\int \psi^*(\mathbf{x},0)\psi(\mathbf{x},t)d\mathbf{x},$$
$$\sigma(\omega)=\omega\,\mathrm{Re}\left\{\int [C(t)\exp i\omega t]dt\right\}. \tag{4.1}$$

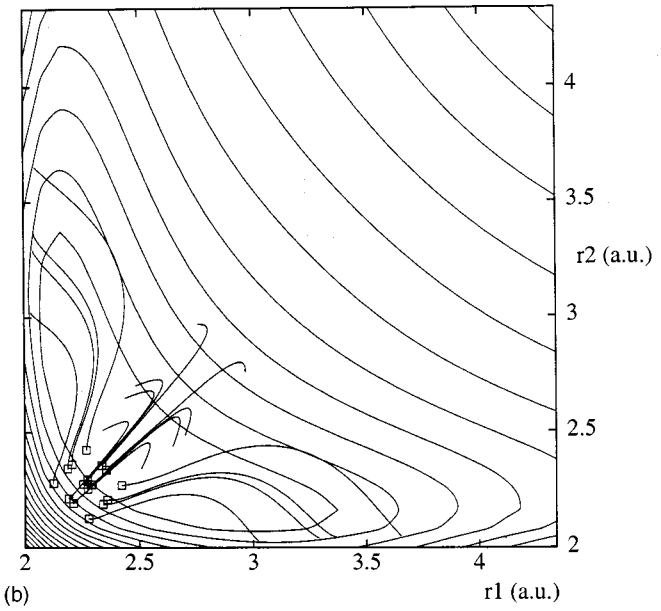
With the QFD representation of the wave function given in Eq. (2.2) as $\psi(\mathbf{x},t)=A(\mathbf{x},t)\exp[iS(\mathbf{x},t)/\hbar]$, $C(t)$ in the above expressions becomes

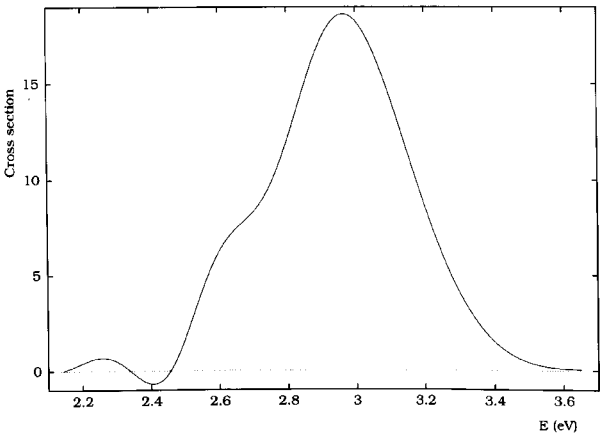
$$C(t)=\int A(\mathbf{x},0)A(\mathbf{x},t)\exp\{i[S(\mathbf{x},t)-S(\mathbf{x},0)]/\hbar\}d\mathbf{x}. \tag{4.2}$$

The dissociation cross section is evaluated in two steps. The spatial integral for the overlap $C(t)$ is followed by the Fourier transform in the time domain. The wave packet is taken to start from rest, with $S(\mathbf{x},0)=A(\mathbf{x},0)$ calculated from the initial wave at the locations of nodes at the time $t=0$. $A(\mathbf{x},t)$ and $S(\mathbf{x},t)$ are given by the numerical calculations. The space integral is calculated by simply multiplying the area of the triangular domains with the values of the









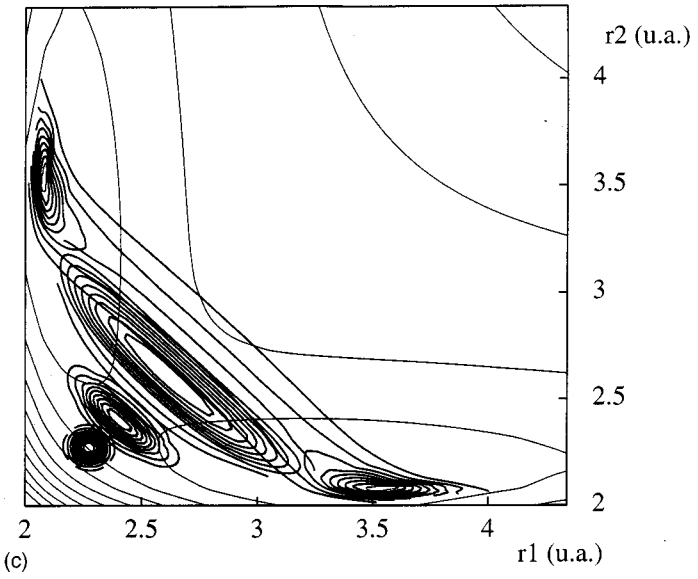


FIG. 2. The dynamics of the NO_2 system with $\theta = \theta_{eq1}$. (a) Evolution of the wave packet represented by snap shots showing the set of discrete points at time $t = 0$, 20, and 40 fs; (b) Sample trajectories corresponding to representative discrete points of the two-dimensional grid; (c) Evolution of the wave packet represented by snap shots showing the set of equal density contours at time $t = 0$, 20, and 40 fs. The evident noise in the plot is a matter of graphical resolution due to the finite number of trajectories; and (d) Time-dependence of the correlation function; and (e) Dissociation cross section as a function of the pump energy in eV.

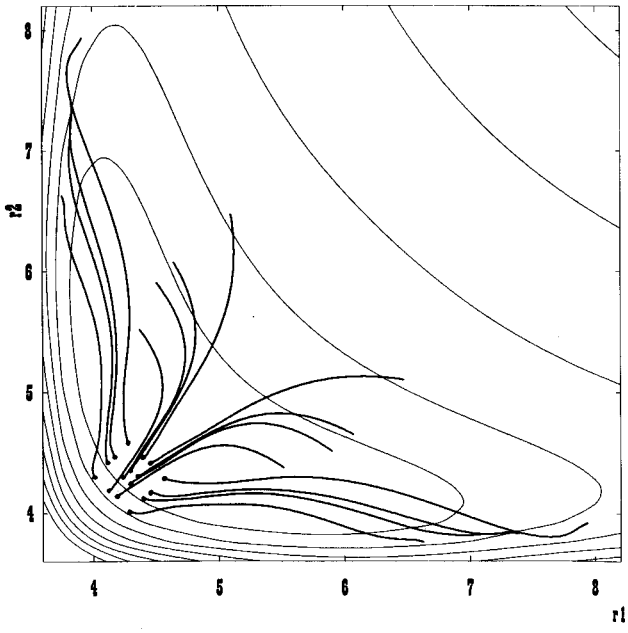


FIG. 3. The dynamics of the NO_2 system with $\theta=\theta_{eq0}$ described by the trajectories corresponding to representative discrete points of the two-dimensional grid over a time span of 40 fs.

integrands at the corners divided by 3. This is equivalent to taking the mean value of the integrand over the triangular domains.

A. The Hamiltonians for NOCl and NO_2

The dynamics of the NOCl system is defined by the Jacobi coordinates R, r, and θ. Here, R is the distance from Cl to the center of mass of NO, r is the vibrational coordinate of NO, and θ is the angle between the vectors $\mathbf{r}$ and $\mathbf{R}$. Similarly, the coordinates r_1, r_2, and θ define the dynamics for NO_2, where r_1 and r_2 denote the distances from N to each of the O atoms. The coordinate θ is the bending angle between the two radial NO directions. In these coordinates, the Hamiltonian for NOCl is defined by[48]

$$\begin{aligned} H\psi=&-\tfrac{1}{2}\hbar^2[(m_dR)^{-1}(R\psi)_{RR}+(m_vr)^{-1}(r\psi)_{rr}\\ &+(I_\theta\sin\theta)^{-1}(\sin\theta\psi_\theta)_\theta]+V(R,r,\theta)\psi,\\ m_d^{-1}=&(m_N+m_O)^{-1}+m_{Cl}^{-1},\quad m_v^{-1}=m_N^{-1}+m_O^{-1},\\ I_\theta^{-1}=&(m_dR^2)^{-1}+(m_vr^2)^{-1}, \end{aligned} \tag{4.3}$$

and the Hamiltonian for NO_2 is defined by[49]

$$\begin{aligned} H\psi=&-\tfrac{1}{2}\hbar^2\{m^{-1}(\psi_{r1r1}+\psi_{r2r2})+(I_\theta\sin\theta)^{-1}(\sin\theta\psi_\theta)_\theta\\ &+2m_N^{-1}\cos\theta\psi_{r1r2}+(m_Nr_1r_2)^{-1}[\cos\theta\sin\theta^{-1}\\ &\times(\sin\theta\psi_\theta)_\theta+\sin\theta^{-1}(\sin\theta(\cos\theta\psi)_\theta)_\theta]\\ &-m_N^{-1}[r_2^{-1}(\sin\theta\psi)_{\theta r1}+r_1^{-1}(\sin\theta\psi)_{\theta r2}]\}\\ &+V(r_1,r_2,\theta)\psi,\\ m^{-1}=&m_N^{-1}+m_O^{-1},\quad I_\theta^{-1}=m^{-1}[r_1^{-2}+r_2^{-2}]. \end{aligned} \tag{4.4}$$

Above, the subscripts in the coordinates indicate the partial derivatives such as $\psi_{r1}=\partial\psi/\partial r_1$, $\psi_{r_1r_1}=\partial^2\psi/\partial r_1^2$; m_N, m_O, and m_{Cl} are, respectively, the masses of the N, O, and Cl atoms; m_d, m_v, and m are reduced masses, and I_θ indicates the moment of inertia for the two cases as defined. The coordinates used and the form of the Hamiltonians are the same for both the S_0 and S_1 potential surfaces for each system. Appropriate potential energy functions V are to be selected according to the electronic state and the particular molecular system.

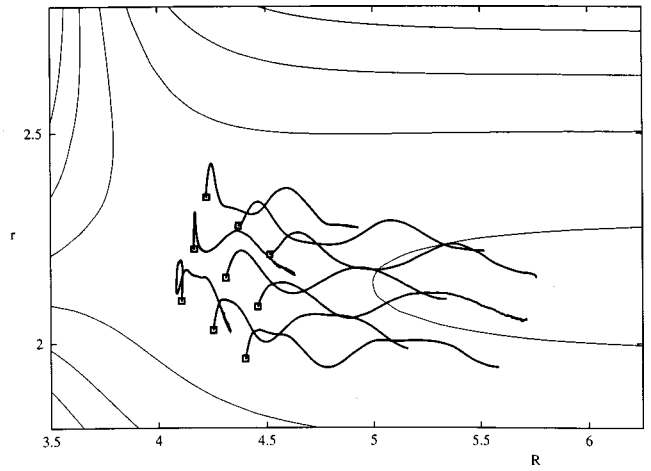


FIG. 4. The dynamics of the NOCl system described by the trajectories corresponding to representative discrete points of the two-dimensional grid over a time span of 40 fs.

As a model for illustration purposes, the θ angle for each case is frozen at a selected equilibrium value θ_{eq}. The simplified Hamiltonians are thus respectively expressed in two radial variables as

$$\begin{aligned} \text{For NOCl:}\quad H\psi=&-(\hbar^2/2)[(m_dR)^{-1}(R\psi)_{RR}\\ &+(m_vr)^{-1}(r\psi)_{rr}]+V(R,r,\theta_{eq})\psi, \end{aligned} \tag{4.5}$$

$$\begin{aligned} \text{For } NO_2\text{:}\quad H\psi=&-(\hbar^2/2m)(\psi_{r1r1}+\psi_{r2r2})\\ &+V(r_1,r_2,\theta_{eq})\psi. \end{aligned} \tag{4.6}$$

For NOCl, the S_0 and S_1 surfaces have the same equilibrium value $\theta_{eq}=127.4°$.[48] For NO_2, the equilibrium value is respectively $\theta_{eq}=133.4°$ and 101.9° on the S_0 and S_1 surfaces.[49] Accordingly, these two values are denoted as θ_{eq0} and θ_{eq1}.

For the calculations, the kinetic energy operators in these simplified Hamiltonians are sought in a common dimensionless representation. The transformations, including the rescaling of the wave function for NOCl, are

$$\begin{aligned} \text{For NOCl:}\quad &\Psi=Rr\psi,\quad V=m_vr_{eq}^2V/\hbar^2,\quad t_0=m_vr_{eq}^2/\hbar,\\ &x=(m_d/m_v)^{1/2}R/r_{eq},\quad y=r/r_{eq},\quad t=t/t_0, \end{aligned} \tag{4.7}$$

$$\begin{aligned} \text{For } NO_2\text{:}\quad &\Psi=\psi,\quad V=mr_{eq}^2V/\hbar^2,\quad t_0=mr_{eq}^2/\hbar,\\ &x=r_1/r_{eq},\quad y=r_2/r_{eq},\quad t=t/t_0. \end{aligned} \tag{4.8}$$

Above, r_{eq} is a length scale taken to be the value of the vibrational coordinate at the molecular equilibrium on the S_0 potential energy surface. For NO_2, r_{eq} is the common value for the two radial coordinates as a result of the symmetry as

$r_{eq}=r_{1eq}=r_{2eq}$. The final expression for the Schrödinger equation for both cases, in the nondimensionalized formulation becomes

$$i\Psi_t=-1/2(\Psi_{xx}+\Psi_{yy})+V(x,y)\Psi. \tag{4.9}$$

This nondimensional form makes it possible to carry out the calculations on both the S_0 and S_1 surfaces for the two molecular systems with a common formulation.

B. Potential energy surfaces

The expressions of the potential energies for the ground and excited electronic states are treated in a unified presentation.

1. S_0 potential energy surface and wave function

The S_0 surface is needed only for determining the ground state wave function to be used as the initial wave packet on the S_1 surface. A quadratic approximation is adequate here for evaluating the molecular ground state. Hence, for both systems, we employ the potential energy

$$V(x,y)=1/2[k_{11}(x-x_{eq})^2+2k_{12}(x-x_{eq})(y-y_{eq}) +k_{22}(y-y_{eq})^2]. \tag{4.10}$$

Above x_{eq} and y_{eq} are the equilibrium values for x and y at the minimum of the potential and are evaluated for the two cases according to the coordinate transformations in Eqs. (4.7) and (4.8). The corresponding ground state is given as

$$\Psi(\mathbf{x},0)=(2\pi\sigma_1\sigma_2)^{-1/2}\exp\{-1/2[a(x-x_{eq})^2 +2b(x-x_{eq})(y-y_{eq})+c(y-y_{eq})^2]\}, \tag{4.11}$$

where a, b, c, σ_1, and σ_2 are obtained from the eigenvalues ω_1^2 and ω_2^2 of the coefficients matrix k_{ij} in Eq. (4.10) and β is the orientation of the eigenvector corresponding to ω_1. The results are

$$\begin{aligned}
&\omega_1^2=\tfrac{1}{2}\{(k_{11}+k_{22})+[(k_{11}-k_{22})^2+4k_{12}^2]^{1/2}\},\\
&\omega_2^2=\tfrac{1}{2}\{(k_{11}+k_{22})-[(k_{11}-k_{22})^2+4k_{12}^2]^{1/2}\},\\
&\tan\beta=2k_{12}/\{(k_{11}-k_{22})+[(k_{11}-k_{22})^2+4k_{12}^2]^{1/2}\},\\
&\sigma_1=(2\omega_1)^{-1/2},\quad \sigma_2=(2\omega_2)^{-1/2},\\
&a=\cos^2\beta/\sigma_1^2+\sin^2\beta/\sigma_2^2,\quad b=\sin\beta\cos\beta/\sigma_1\sigma_2,\\
&c=\sin^2\beta/\sigma_1^2+\cos^2\beta/\sigma_2^2.
\end{aligned} \tag{4.12}$$

The numerical values of the coefficients k_{ij} in the quadratic potentials of the two cases are derived in Appendix B from the general expressions for the potential energies for S_0.

2. S_1 potential energy surfaces

The S_1 potential energy surfaces are presented in Appendix C for the NOCl and NO_2 systems. Two-dimensional representations are derived by fixing $\theta_{eq}=127.4°$ for NOCl and at, respectively, the two different values $\theta_{eq0}=133.4°$ and $\theta_{eq1}=101.9°$ for NO_2 in order to explore the dependence of the dynamics on θ.

V. DISCUSSION

The results of the calculations are presented in terms of the evolution of the initial wave packet, the correlation function of the wave packet and the dissociation cross section for the NOCl→NO+Cl and NO_2→NO+O reactions. Three complementary formats are chosen for displaying the dynamics of the wave packet: snapshots of the assembly of ''quantum fluid particles'' obtained through the discretization of the continuum equations; snapshots of equal probability density contours; and the trajectories of representative particles. The numerical results for the wave packet dynamics and dissociation cross sections are given in Figs. 2–4.

The initial locations of the particles are obtained from the discretization of the ground state Gaussian wave function. This is achieved by first writing the initial Gaussian for the density as the product of Gaussians in one variable in the principal axes of the quadratic potential. In each direction, N subregions of equal area under the density function are determined.[12] The two subregions at the edges in each direction are semi-infinite, and thus the discretization covers the whole space. The boundaries $\{X_j\}$ of the segments divide the two-dimensional space into regions of different sizes, but of equal ''mass,'' in the fluid dynamics analogy. For instance, in the coordinate x with N intervals, $\int_{X_j}^{X_{j+1}}\exp(-x^2/2\omega_1^2)dx/(2\pi)^{1/2}\omega_1=1/N$. The center of mass x_j of this subregion provides the corresponding coordinate of the quantum subparticle as $\int_{X_j}^{X_{j+1}}x\exp(-x^2/2\omega_1^2)dx/(2\pi)^{1/2}\omega_1=x_j/N$. Furthermore, by construction, the particles in the numerical calculations occupy the center of gravity of each rectangular region at the initial time. The consequence of taking the rectangular areas to have the same mass and assigning this mass to the particle at the center of gravity attaches equal importance to each particle and places them more densely in the regions of higher probability. Pictorially, this is reflected in Fig. 2 by particles being unequally spaced: more dense at the center and sparse at the edges. Typically, the spacing at the edges is about 3.5 of that at the center. The grid used in the actual calculations for each of the three cases had 19 points in both the x and y directions. The calculations are completed in 1504 and 864 time steps, respectively, for the NOCl and NO_2 cases as displayed by the decay of the correlation functions, such as in Fig. 2(d).

A complete set of figures are presented for describing the dynamics in the photodissociation reaction for NO_2 with the bending angle kept at the equilibrium value $\theta_{eq}=133.4°$ of the S_0 surface. Figures 2(a)–2(c) describe, respectively, (a) the evolution of the wave packet by snapshots of the locations of the set of discrete points at time $t=0$, 20, and 40 fs, (b) representative trajectories corresponding to sixteen discretized points of the two-dimensional grid, and (c) snapshots showing the set of equal density contours at time $t=0$, 20, and 40 fs. Figures 2(d) and 2(e) show, respectively, the correlation of the wave function in time and the corresponding dissociation cross-section in terms of the pump energy. Similarly, Figs. 3 and 4 show representative trajectories for the photodissociation reactions for respectively NO_2 with the bending angle $\theta_{eq}=101.9°$ kept at the

equilibrium value of the S_1 surface, and for NOCl with Jacobi's angle fixed at the value $\theta_{eq}=127.4°$.

The wave packet appears like a droplet in the hydrodynamics analogy. The classical picture is the motion of the ensemble of particles forming the droplet on the S_1 surface, starting from the configuration corresponding to the initial wave function prepared on the S_0 surface. The motion of the wave packet consists of its dispersion and sliding down the surface described by the level curves in the figures. The energy surfaces in Figs. 2 and 3 for NO_2, corresponding respectively to the bending angle values of and $\theta=\theta_{eq0}$ and $\theta=\theta_{eq1}$, are symmetric with respect to the bisector of the first quadrant reflecting the symmetry of the system with respect to the two NO intramolecular distances. For the first case in Fig. 2, the potential energy surface has a ridge on the symmetry line and two shallow wells on the two sides of the ridge. Consequently, the wave packet starting from rest, initially moves along the ridge, eventually splits into two and flows down into the wells. The potential surface in Fig. 3 corresponding to NO_2 with $\theta=\theta_{eq1}$ has a large shallow symmetric well and no ridge. The wave packet placed over the top, initially flows down into the large well, and also eventually splits into two and each piece splashes onto one of the walls of the well. The S_1 surface in Fig. 4 for NOCl consists of a simple valley with a downward slope. Consequently, the dissociation dynamics is also simpler; the initial wave packet placed over the top slides down the slope with minor sideways oscillations and expands in time. For this case, the wave packet stays together throughout the process as opposed to the breaking of the initial wave packet into two smaller ones in the two former cases. For all cases, the detailed behavior of the wave packets, and the peaks and width of the dissociation cross section are comparable with the results of the full three-dimensional calculations,[48,49] as well as the calculations based on the Eulerian description of QFD.[42]

The goal of the calculations presented here is primarily for illustration of the associated numerical algorithm without the pretense of an exhaustive physical study. These calculations, including the evaluation of the dissociation cross section took, respectively, 33 s for the NOCl and 40 s for each of the NO_2 cases on a Pentium 200 MHz PC. The computational efficiency of the QFD calculations of this paper is assessed in the following through references with other methods. To summarize, the duration of the photodissociation dynamics for NOCl and NO_2 cases are, respectively, 34 and 38 fs in the QFD calculations of this paper. These calculations are carried out respectively in 1504 and 864 discrete time steps. The CPU times for running these cases on a Pentium 200 MHz machine were, respectively, 33 and 40 s. Hence, the discrete time steps used in the calculations are approximately 0.02 fs for NOCl and 0.04 fs for NO_2. The resulting CPU times per each time step thus became approximately 0.02 and 0.05 s. The values for both the discrete time steps and CPU times per time step are seen to be of the same order for the two reactions, with ratios of about 2. The minor differences in the number of time steps and the CPU times per time step can be explained in terms of the potential surfaces for the two chemical systems. The potential energy function for NOCl is expressed by much fewer terms than the one for NO_2. Consequently, more time is spent in calculating the potential energy values for NO_2 than for NOCl. This explains the 2.5 times longer computational effort (i.e., the larger CPU per time step for the NO_2 reaction). On the other hand, although the potential energy surface for NOCl is simpler than for NO_2, it is stiffer for the molecular stretch modes (i.e., the walls of the valley of the potential energy surface rise more rapidly in the vibrational coordinate). This causes the program to proceed with smaller time steps in order to accommodate for the stiffer potential, and the discrete time step for NOCl becomes half that for NO_2. The same physical problems in this paper are studied in their full three-dimensional versions by the multiconfiguration time-dependent Hartree method.[48,49] The CPU times for these are reported to be about 1 h for NOCl and 45 min to 3 days for various levels of convergence for NO_2 on an IRIS 4D-320 RISC workstation. For the NO_2 case, the authors report that the CPU time for a fully converged calculation would have been 2 months.[49] We refrain from comparing the results with the problems in two and three coordinates. Nevertheless, the large margin of two orders of magnitude for NOCl and two to three, or even five orders of magnitude for the reported time necessary for fully converged calculations is encouraging for the potential capability of the QFD formulation. Towards obtaining a more direct reference on efficiency, the problems in two Cartesian coordinates of this paper are integrated using the commonly employed Chebychev FFT method.[32] Two sets of computations are carried for both systems with the FFT. In a first set of computations, the NOCl and NO_2 cases are integrated in the same number of time steps (1504 and 864 steps, respectively), as in the present paper. The CPU times with the FFT algorithm were respectively 110 and 90 min for the two problems on the same PC. The regions of the potential energy surfaces used in these calculations were $\{3.5\,\text{a.u.}<R<6.75\,\text{a.u.}, 1.8\,\text{a.u.}<r<2.8\,\text{a.u.}\}$ for NOCl and $\{3.4\,\text{a.u.}<rl<8.4\,\text{a.u.}$, same for $r2\}$ for NO_2. In both systems, the regions are discretized on a 128×128 grid. The comparison of the total CPU times leads to a ratio of two orders of magnitude in favor of QFD. In another set of computations, we tried to optimize the advantages of the FFT algorithm by taking the largest allowable time steps. These calculations were carried out respectively in 30 and 40 discrete time steps for the NOCl and NO_2 cases. The corresponding total CPU times for the two computations are about 1460 and 1470 s, respectively. These times are of course smaller than before. However due to the iterative nature of the FFT method, the reduction with time is not proportional to the number of steps. For the bigger time steps, the series in Chebychev polynomials takes a longer time to converge as compared to the smaller time steps. The comparison of the total CPU times in these latter calculations benefiting from the large time step capability of the FFT, is still in favor of QFD method by the factors of 50–40. Another comparison may be carried with respect to the CPU times per time step between the FFT and QFD calculations. By dividing the total CPU times by the number of steps, the values of 4 and 6 s are found for the large number (i.e., shorter time steps for the FFT calculations). Similarly, the CPU times per time step are found to be 50 and 40 s for

calculations with the smaller number of steps. The corresponding values are, respectively, the 0.02 and 0.05 s with QFD as quoted above. These lead to a ratio of about two and three orders of magnitude depending on the large or small numbers of steps for both reactions in favor of QFD. As in all comparisons of this nature, care is recommended in reaching strong conclusions. Regardless of the specific ratios of speed in the analysis, the capabilities of the present algorithm are most encouraging.

For time-independent problems, stability and accuracy considerations determine the value of the discrete time step. Time-dependent problems with oscillating external fields are frequently encountered in many applications. In these cases, the time variation of the external field can determine the discrete time step. Hence, most algorithms, including the FFT method, can no longer utilize large time steps. An additional comment regards the FFT method capitalizing on the Cartesian coordinate representation of the kinetic energy operator. The trajectories in the Lagrangian formulation of QFD can be calculated in any coordinate system. Finally, the Lagrangian formulation as an adaptive moving grid does not involve concerns about reflection from boundaries as is the case with fixed grid methods.

The QFD, Lagrangian description and the explicit time integrator collectively lead to the observed computational efficiency. QFD permits working with the near monotonous discretized amplitude and phase. This is most clearly displayed by the simple nature of the trajectories seen in Figs. 2 and 3. The reduction of the number of discrete points as compared to what would be needed to represent the oscillatory real and imaginary parts of the complex wave function is expected to be at least an order of magnitude in each direction. The near monotonous variations of the phase and velocity fields are verified and contrasted with the oscillatory behavior of the real and imaginary parts of the complex wave function in Ref. 42, in support of this statement. The Lagrangian approach of following the particles, concentrates the computational effort into the regions of space with high probability density. In this respect, the Lagrangian scheme is an optimal adaptive grid algorithm. Similarly, the Lagrangian approach eliminates the problems associated with the reflection of waves from the boundaries of a finite region found with the fixed grid methods. Finally, the explicit integrator makes the effort linearly proportional to the number of discrete points.

APPENDIX A: SPATIAL DERIVATIVES ON AN IRREGULAR MESH

The goal is to calculate the partial derivatives f_x, f_y and the Laplacian $f_{xx}+f_{yy}$ at the nodes of an irregular grid. Figure 1 shows the irregular polygon defined by eight corners and an interior point that is used in the calculations. The present formulation benefits from the numerical techniques in the field of finite elements[26,58–62] that map the irregular cells onto a square in an auxiliary space. In this second space with the simple geometry for the cells, straight forward local interpolation approximations of the relevant functions permit the numerical evaluation of the derivatives.[59,60]

1. The interpolation functions

The coordinates x, y, and the function $f(x,y)$ are interpolated from the nodal values of the finite clement shown in Fig. 1. For this purpose, the row vectors **X**, **Y**, and **F** are introduced as

$$
\begin{aligned}
&<\mathbf{X}=(x_0,x_1,x_2,x_3,x_4,x_5,x_6,x_7,x_8),\\
&<\mathbf{Y}=(y_0,y_1,y_2,y_3,y_4,y_5,y_6,y_7,y_8),\\
&<\mathbf{F}=(f_0,f_1,f_2,f_3,f_4,f_5,f_6,f_7,f_8).
\end{aligned}
\tag{A1}
$$

Above (x_k,y_k) represent the nine points of the polygon as shown in Fig. 1 and similarly $f_k=f(x_k,y_k)$ is the value of the function at the nodes.

The interpolations are introduced by the auxiliary coordinates ξ, η, and basis vectors $\mathbf{b}(\xi,\eta)$ as

$$
\begin{aligned}
&x=x(\xi,\eta)=\langle\mathbf{b}(\xi,\eta)|\mathbf{X}\rangle,\\
&y=y(\xi,\eta)=\langle\mathbf{b}(\xi,\eta)|\mathbf{Y}\rangle,\\
&f=f(\xi,\eta)=\langle\mathbf{b}(\xi,\eta)|\mathbf{F}\rangle.
\end{aligned}
\tag{A2}
$$

The choice of the same basis **b** for the function f and the coordinates x, y is defined as an isoparametric mapping.[59,60] The interior point of the polygon in the (x,y) plane and of the square in the (ξ,η) plane is labeled by the index 0 and the corners as 1–8. The points of the square in the (ξ,η) plane are, respectively, defined by the coordinates (0, 0); (1, 0); (−1, 0); (0, 1); (0, −1); (1, 1); (−1, −1); (−1, 1); (1, −1). The basis vector **b** for this element is[58]

$$
\begin{aligned}
&<\mathbf{b}(\xi,\eta)=[(1-\xi^2)(1-\eta^2),\\
&\xi(1+\xi)(1-\eta^2)/2,\quad -\xi(1-\xi)(1-\eta^2)/2,\\
&\eta(1+\eta)(1-\xi^2)/2,\quad -\eta(1-\eta)(1-\xi^2)/2,\\
&\xi\eta(1+\xi)(1+\eta)/4,\quad \xi\eta(1-\xi)(1-\eta)/4,\\
&-\xi\eta(1-\xi)(1+\eta)/4,\quad -\xi\eta(1+\xi)(1-\eta)/4].
\end{aligned}
\tag{A3}
$$

It is readily observed that at the points of the square in the (ξ,η) plane $b_j(\xi_k,\eta_k)=\delta_{jk}$, where δ_{jk} is the Kronecker delta. Other element types and the associated transformations for both two- and three-dimensional spaces can be found in the literature.[59,60]

2. The first order partial derivatives

The chain rule for the partial derivatives of the typical function $f=f(x,y)$ with the coordinate transformation from x, y to ξ, η reads

$$
\begin{aligned}
&f_x=f_\xi\xi_x+f_\eta\eta_x,\\
&f_y=f_\xi\xi_y+f_\eta\eta_y.
\end{aligned}
\tag{A4}
$$

The inverses $\xi=\xi(x,y)$ and $\eta=\eta(x,y)$ of the transforms in Eq. (A2) are not available explicitly for the direct computation of the derivatives ξ_x, ξ_y, η_x, and η_y appearing in the chain rules above. Nevertheless, these partial derivatives can be obtained from x_ξ, x_η, y_ξ, and y_η by a matrix inversion. The partial derivatives of the expressions $x=x(\xi,\eta)$ and y

$=y(\xi,\eta)$ with respect to x and y obtained via the chain rule, result in four expressions that are arranged in a matrix form $\mathbf{J}\cdot\mathbf{J}^{-1}=\mathbf{I}$,

$$\mathbf{J}=\begin{pmatrix} x_\xi & x_\eta \\ y_\xi & y_\eta \end{pmatrix}, \quad \mathbf{J}^{-1}=\begin{pmatrix} \xi_x & \xi_y \\ \eta_x & \eta_y \end{pmatrix}. \tag{A5}$$

Here, $\mathbf{I}$ is the identity matrix; $\mathbf{J}$ and $\mathbf{J}^{-1}$ are, respectively, the Jacobian matrix of the coordinate transformation $x=x(\xi,\eta)$, $y=y(\xi,\eta)$ and its inverse. The inversion of the $\mathbf{J}$ matrix in Eq. (A5) yields the partial derivatives ξ_x, ξ_y, η_x, and η_y as

$$\mathbf{J}^{-1}=\begin{pmatrix} \xi_x & \xi_y \\ \eta_x & \eta_y \end{pmatrix}=\begin{pmatrix} y_\eta & -x_\eta \\ -y_\xi & x_\xi \end{pmatrix}/J, \tag{A6}$$

where J is the Jacobian of the transformation,

$$J=\det\mathbf{J}=(x_\xi y_\eta - x_\eta y_\xi). \tag{A7}$$

Hence, Eq. (A6) shows that the partial derivatives ξ_x, ξ_y, η_x, and η_y are obtained without the need to know the inverse transformations $\xi=\xi(x,y)$ and $\eta=\eta(x,y)$. The partial derivatives with the chain rule expressions in Eq. (A4) can be written in the compact form

$$\nabla_x f=\mathbf{J}^{-1}\cdot\nabla_\xi f, \tag{A8}$$

where $\nabla_x f=(f_x,f_y)$ and $\nabla_\xi f=(f_\xi,f_\eta)$ denote, respectively, the column vectors with the components of the gradient in the respective coordinates.

The partial derivatives in the (ξ,η) space are readily calculated from the derivatives of $\mathbf{b}(\xi,\eta)$ with respect to the ξ and η coordinates according to Eq. (A2) and (A3) as

$$\begin{aligned} &x_\xi=\langle\mathbf{b}_\xi|\mathbf{X}\rangle, \quad x_\eta=\langle\mathbf{b}_\eta|\mathbf{X}\rangle, \\ &y_\xi=\langle\mathbf{b}_\xi|\mathbf{Y}\rangle, \quad y_\eta=\langle\mathbf{b}_\eta|\mathbf{Y}\rangle, \\ &f_\xi=\langle\mathbf{b}_\xi|\mathbf{F}\rangle, \quad f_\eta=\langle\mathbf{b}_\eta|\mathbf{F}\rangle. \end{aligned} \tag{A9}$$

$\mathbf{b}_\xi$ and $\mathbf{b}_\eta$ are calculated in a straightforward manner in view of the expression of $\mathbf{b}$ in Eq. (A3). At the central point with the coordinates $\xi=0$, $\eta=0$,

$$\begin{aligned} &<\mathbf{b}_\xi=[0,\ 1/2,\ -1/2,\ 0,\ 0,\ 0,\ 0,\ 0,\ 0], \\ &<\mathbf{b}_\eta=[0,\ 0,\ 0,\ 1/2,\ -1/2,\ 0,\ 0,\ 0,\ 0], \\ &x_\xi=(x_1-x_2)/2, \quad x_\eta=(x_3-x_4)/2, \\ &y_\xi=(y_1-y_2)/2, \quad y_\eta=(y_3-y_4)/2, \\ &f_\xi=(f_1-f_2)/2, \quad f_\eta=(f_3-f_4)/2, \\ &J=[(x_1-x_2)(y_3-y_4)-(x_3-x_4)(y_1-y_2)]/4. \end{aligned} \tag{A10}$$

The above expressions are seen to reduce to the simple centered finite differentiation formulas.

The partial derivatives of $f(x,y)$ in the (x,y) plane are obtained with the substitution of f_ξ, f_η from above and the expressions for ξ_x, ξ_y, η_x, and η_y from Eq. (A6) into Eq. (A9). In particular at the central point, combining the expressions given in Eq. (A10), these yield

$$\begin{aligned} &f_x=4[(f_1-f_2)(y_3-y_4)-(f_3-f_4)(y_1-y_2)]/J, \\ &f_y=4[(f_1-f_2)(x_3-x_4)-(f_3-f_4)(x_1-x_2)]/J. \end{aligned} \tag{A11}$$

The derivatives at the edges are evaluated by first making extrapolations to generate additional points. The extrapolations transform the edge points to become interior nodes and the same formulas as above are used.

3. The divergence and the Laplacian

The divergence of a vector function $\mathbf{u}=(u,v)$ are obtained by the use of the above derivative formulas in the x and y components as required by the definition $\nabla\cdot\mathbf{u}=u_x+v_y$. Similarly, the terms f_{xx} and f_{yy} forming the Laplacian $\nabla^2 f=f_{xx}+f_{yy}$ are evaluated by using the first order derivative formulas above twice.

APPENDIX B: S_0 surface for NOCl and NO_2

The S_0 surfaces typically have a deep well and the quadratic approximation is considered as adequate for the evaluation of the molecular ground state for the purposes here. Hence, for both systems, we seek the potential energy expressions in the form

$$\begin{aligned} V(x,y)=1/2[&k_{11}(x-x_{\rm eq})^2+2k_{12}(x-x_{\rm eq})(y-y_{\rm eq}) \\ &+k_{22}(y-y_{\rm eq})^2]. \end{aligned} \tag{B1}$$

Above $x_{\rm eq}$ and $y_{\rm eq}$ are the equilibrium values for x and y defined suitably for the two cases in Eqs. (4.7) and (4.8).

1. S_0 surface for NOCl

The potential energy is given in dimensional units in terms of r_1, r_2, and r_3 which are, respectively, the NO, NCl, and OCl distances[48] as

$$\begin{aligned} V(r_1,r_2,r_3)=1/2&\sum_{i=1}^{3} k_i(r_i-r_{1\rm eq})^2 \\ &+k_{23}(r_2-r_{2\rm eq})(r_3-r_{3\rm eq}). \end{aligned} \tag{B2}$$

The coordinates r_1, r_2, and r_3 are related to the dynamical coordinates R, r, and θ as[48]

$$\begin{aligned} &r_1=r, \\ &r_2^2=[m_{\rm O}/(m_{\rm O}+m_{\rm N})]^2 r^2+R^2 \\ &\quad +2[m_{\rm O}/(m_{\rm O}+m_{\rm N})]\cos\theta Rr, \\ &r_3^2=[m_{\rm N}/(m_{\rm O}+m_{\rm N})]^2 r^2+R^2 \\ &\quad -2[m_{\rm N}/(m_{\rm O}+m_{\rm N})]\cos\theta Rr. \end{aligned} \tag{B3}$$

The inverse relations to these are

$$\begin{aligned} &r=r_1, \\ &R^2=-[m_{\rm N}m_{\rm O}/(m_{\rm O}+m_{\rm N})^2]r_1^2+[m_{\rm N}/(m_{\rm O}+m_{\rm N})]r_2^2 \\ &\quad +[m_{\rm O}/(m_{\rm O}+m_{\rm N})]r_3^2, \end{aligned} \tag{B4}$$

$$\cos\theta=\{[(m_{\rm N}-m_{\rm O})/(m_{\rm O}+m_{\rm N})]r_1^2+r_2^2-r_3^2\}/2Rr.$$

For obtaining a quadratic representation of the potential in terms of the dynamical coordinates R, r, and $\theta=\theta_{\rm eq}$ a Taylor

series of the coordinates r_2 and r_3 about their equilibrium values is considered. The result in the leading order is

$$r_2 - r_{2eq} = A(R - R_{eq}) + B(r - r_{eq}),$$
$$r_3 - r_{3eq} = C(R - R_{eq}) + D(r - r_{eq}), \tag{B5}$$

where R_{eq} and r_{eq} are obtained by substituting the equilibrium values for r_1, r_2, and r_3 in Eq. (B4) and

$$A = \partial r_2/\partial R|_{eq} = \{R_{eq} + [m_O/(m_O + m_N)]\cos\theta_{eq} r_{eq}\}/r_{2eq},$$
$$B = \partial r_2/\partial r|_{eq} = [m_O/(m_O + m_N)]\{\cos\theta_{eq} R_{eq} + [m_O/(m_O + m_N)] r_{eq}\}/r_{2eq},$$
$$C = \partial r_3/\partial R|_{eq} = \{R_{eq} - [m_N/(m_O + m_N)]\cos\theta_{eq} r_{eq}\}/r_{3eq}, \tag{B6}$$
$$D = \partial r_3/\partial r|_{eq} = [m_N(m_O + m_N)]\{-\cos\theta_{eq} R_{eq} + [m_N/(m_O + m_N)] r_{eq}\}/r_{3eq}.$$

The dimensionless coefficients of the ground state potential energy surface in the quadratic representation as given in Eq. (B1), in view of the coordinate transformations in Eq. (B4) become

$$k_{11} = (m_v r_{eq}^2 R_{eq}^2/\hbar^2)(A^2 k_2 + C^2 k_3 + 2AC k_{23}),$$
$$k_{22} = (m_v r_{eq}^4/\hbar^2)(k_1 + B^2 k_2 + D^2 k_3 + 2BD k_{23}), \tag{B7}$$
$$k_{12} = (m_v r_{eq}^3 R_{eq}/\hbar^2)[AB k_2 + CD k_3 + (AD + BC) k_{23}].$$

The numerical values for the coefficients in atomic units are[48]

$$r_{1eq} = 2.155, \quad r_{2eq} = 3.729, \quad r_{3eq} = 4.989,$$
$$R_{eq} = 4.3137, \quad r_{eq} = 2.155, \quad \theta_{eq} = 127.4°,$$
$$k_1 = 0.8987, \quad k_2 = 0.0874, \quad k_3 = 0.1137, \tag{B8}$$
$$k_{23} = 0.0122, \quad m_d = 29661, \quad m_v = 13710.$$

Hence, the dimensionless values in the potential defined in Eq. (B1) and the parameters of the corresponding Gaussian for the ground state wave function given in Eq. (4.11) become

$$x_{eq} = 2.944, \quad y_{eq} = 1(\text{by definition}),$$
$$k_{11} = 0.256 \times 10^6, \quad k_{22} = 0.267 \times 10^6,$$
$$k_{12} = 0.013 \times 10^6,$$
$$\omega_1 = 0.525 \times 10^3, \quad \omega_2 = 0.498 \times 10^3, \tag{B9}$$
$$\sigma_1 = 0.0309, \quad \sigma_2 = 0.0317, \quad \beta = 1.03\,\text{rad} = 59°.2,$$
$$A = 0.9696, \quad B = -0.2103, \quad C = 0.9871,$$
$$D = 0.3391.$$

The time scale [i.e., the unit of dimensionless time t_0 defined in Eq. (4.7)] is 1.54 ps.

2. S_0 surface for NO_2

The potential energy is given in terms of the two NO interatomic distances r_1, r_2, and the bending angle θ. The quadratic approximation to the potential about the equilibrium values for r_1, r_2, and $\theta = \theta_{eq}$ is [49]

$$V(r_1, r_2) = c_2[(r_1 - r_{eq})^2 + (r_2 - r_{eq})^2] + c_{11}(r_1 - r_{eq})(r_2 - r_{eq}). \tag{B10}$$

Above, r_{eq} denotes the common equilibrium value for r_1 and r_2. Using the transformation in Eq. (4.7), the dimensionless coefficients k_{ij} of the quadratic approximation in Eq. (B1) become

$$k_{11} = k_{22} = (m r_{eq}^4/\hbar^2) c_{20}, \quad k_{12} = (m r_{eq}^4/\hbar^2) c_{11}. \tag{B11}$$

The numerical values for the coefficients in atomic units are[49]

$$r_{eq} = 2.27, \quad \theta_{eq} = 133.63°, \quad m = 13710,$$
$$c_{20} = 0.1261, \quad c_{11} = 0.0659. \tag{B12}$$

Hence, the dimensionless values in the quadratic potential in Eq. (B1) and the parameters of the corresponding Gaussian for the ground state wave function given in Eq. (4.11) become

$$x_{eq} = y_{eq} = 1(\text{by definition}),$$
$$k_{11} = k_{22} = 0.459 \times 10^6, \quad k_{12} = 0.240 \times 10^5,$$
$$\omega_1 = 0.264 \times 10^3, \quad \omega_2 = 0.148 \times 10^3, \tag{B13}$$
$$\sigma_1 = 0.0435, \quad \sigma_2 = 0.0581, \quad \beta = 45°(\text{by symmetry}).$$

The time scale [i.e., the unit of dimensionless time t_0 defined in Eq. (4.8)], is 6.11 ps.

APPENDIX C: S_1 SURFACE FOR NOCl AND NO_2

The calculations are carried out in nondimensional variables.

1. S_1 surface for NOCl

V is taken as[48]

$$V = a_2(r - r_{eq})^2 + [1 - Q(R)][c_{00} + c_{01}Q(R) + c_{10}(r - r_{eq}) + c_{20}(r - r_{eq})^2 + c_{11}Q(R)(r - r_{eq}) + c_{21}Q(R)(r - r_{eq})^2], \tag{C1}$$

where

$$Q(R) = 1 - \exp[-\alpha(R - R_{eq})]. \tag{C2}$$

The potential in Eq. (C1) is a simplified form as compared with the more general expression given in Ref. 48 and the values for the coefficients in atomic units are

$$R_{eq} = 4.315, \quad r_{eq} = 2.136, \quad \theta_{eq} = 127.4°$$
$$\alpha = 1.5, \quad a_2 = 0.6816,$$
$$c_{00} = 0.03848, \quad c_{10} = -0.05587, \quad c_{01} = 0.008342, \tag{C3}$$
$$c_{20} = -0.163186, \quad c_{11} = 0.058217, \quad c_{21} = -0.0290674.$$

The nondimensionalized form of the potential energy in Eq. (C1) becomes

$$V = a_2(y - y_{eq})^2 + c_{00}[1 - Q(x)] \times [1 + c_{01}Q(x) + c_{10}(y - y_{eq}) + c_{20}(y - y_{eq})^2 + c_{11}Q(x)(y - y_{eq}) + c_{21}Q(x)(y - y_{eq})^2], \tag{C4}$$

with

$$Q(x)=1-\exp[-\alpha(x-x_{\mathrm{eq}})], \tag{C5}$$

where x and y are defined in Eq. (4.7) and the dimensionless values of the parameters are

$$\begin{aligned}
&x_{\mathrm{eq}}=2.945, \quad y_{\mathrm{eq}}=0.991,\\
&a_2=(m_v r_{\mathrm{eq}}^4/\hbar^2)a_2=0.202\times 10^6, \quad \alpha=\alpha r_{\mathrm{eq}}=3.204,\\
&c_{00}=(m_v r_{\mathrm{eq}}^2/\hbar^2)c_{00}=2450,\\
&c_{10}=r_{\mathrm{eq}}c_{10}/c_{00}=-3.129, \quad c_{01}=c_{01}/c_{00}=0.217,\\
&c_{20}=r_{\mathrm{eq}}^2 c_{20}/c_{00}=-19.69, \quad c_{11}=r_{\mathrm{eq}}c_{11}/c_{00}=3.260,\\
&c_{21}=r_{\mathrm{eq}}^2 c_{21}/c_{00}=-3.508.
\end{aligned} \tag{C6}$$

2. S_1 surface for NO_2

V is taken as[49]

$$V=V_{\mathrm{NO}}(r_1)+V_{\mathrm{NO}}(r_2)+\exp-\alpha[(r_1-r_{\mathrm{eq}})+(r_2-r_{\mathrm{eq}})]\sum b_{klm}Q(r_1)^k Q(r_2)^1 T(\theta)^m, \tag{C7}$$

where

$$\begin{aligned}
&Q(r)=1-\exp[-\alpha(r-r_{\mathrm{eq}})],\\
&V_{\mathrm{NO}}(r)=a_2Q^2(r)+a_3Q^3(r)+a_4Q^4(r),\\
&T(\theta)=c_1(\theta-\theta_{\mathrm{eq1}})+c_2(\theta-\theta_{\mathrm{eq1}})^2+c_3(\theta-\theta_{\mathrm{eq1}})^3,
\end{aligned} \tag{C8}$$

and θ_{eq1} the equilibrium value of the bending angle θ for the S_1 surface.

The numerical values of the coefficients in Eq. (C8) are given below in atomic units, except for c_1, c_2, and c_3 that are already nondimensional[49]

$$\begin{aligned}
&\theta_{\mathrm{eq1}}=101°.89, \quad r_{\mathrm{eq}}=2.44, \quad \alpha=1,\\
&a_2=0.109848, \quad a_3=-0.15567, \quad a_4=0.154428,\\
&c_1=1.2811, \quad c_2=-0.265, \quad c_3=-0.10.
\end{aligned} \tag{C9}$$

The coefficients b_{klm} have the symmetry $b_{klm}=b_{1km}$ and the indices k, l, m range from 0 to 4. The nonvanishing elements of b_{klm} entering in Eq. (C7) are[49]

$$\begin{aligned}
&b_{000}=0.029568, \quad b_{010}=0.029568, \quad b_{020}=0.029568,\\
&b_{030}=0.029568, \quad b_{040}=0.029568, \quad b_{110}=0.254150,\\
&b_{120}=0.136002, \quad b_{130}=0.046866, \quad b_{140}=0.145965,\\
&b_{220}=-0.130562, \quad b_{230}=-0.102040,\\
&b_{011}=0.053373, \quad b_{021}=0.007683,\\
&b_{031}=0.007603, \quad b_{041}=0.003994,\\
&b_{111}=0.054133, \quad b_{121}=-0.004434,\\
&b_{131}=-0.005593, \quad b_{221}=0.026411,\\
&b_{002}=0.146273, \quad b_{012}=0.004513,\\
&b_{022}=0.017309, \quad b_{032}=0.031238,\\
&b_{112}=0.045356, \quad b_{122}=0.045440,\\
&b_{003}=-0.040799, \quad b_{013}=0.039663,\\
&b_{023}=0.003209, \quad b_{113}=0.073022,\\
&b_{004}=0.116980, \quad b_{014}=0.046287.
\end{aligned} \tag{C10}$$

The nondimensionalized forms of the potential and the accompanying coefficients become

$$V=V_{\mathrm{NO}}(x)+V_{\mathrm{NO}}(y)+\exp\{-\alpha[(x-x_{\mathrm{eq}})+(y-y_{\mathrm{eq}})]\}\sum b_{klm}Q(x)^k Q(y)^1 T(\theta_{\mathrm{eq}})^m, \tag{C11}$$

where $T(\theta)$ defined in Eq. (C8) is already nondimensional and

$$\begin{aligned}
&Q(x)=1-\exp[-\alpha(x-x_{\mathrm{eq}})],\\
&V_{\mathrm{NO}}(x)=a_2Q(x)^2+a_3Q(x)^3+a_4Q(x)^4.
\end{aligned} \tag{C12}$$

The numerical values of the above coefficients in dimensionless units are

$$\begin{aligned}
&x_{\mathrm{eq}}=y_{\mathrm{eq}}=1.063, \quad \alpha=\alpha r_{\mathrm{eq}}=2.41,\\
&b_{klm}=(mr_{\mathrm{eq}}^2/\hbar^2)b_{klm}, \quad a_2=(mr_{\mathrm{eq}}^2/\hbar^2)a_2=14667,\\
&a_3=(mr_{\mathrm{eq}}^2/\hbar^2)a_3=-20786, \quad a_4=(mr_{\mathrm{eq}}^2/\hbar^2)a_4=20619.
\end{aligned} \tag{C13}$$

For this system, the S_0 and S_1 surfaces have different equilibrium values, respectively, as $\theta_{\mathrm{eq0}}=133.4°$ and $\theta_{\mathrm{eq1}}=101.9°$. To explore the dependence of the dynamics on θ, the potential V is evaluated for each of these angles, and correspondingly, two sets of numerical studies are conducted. Hence, setting θ as equal to θ_{eq1}, only the terms with $m=0$ remain in the summation in Eq. (C7) while all $m=0$, 1, 2, 3, and 4 contribute with $\theta=\theta_{\mathrm{eq0}}$.

ACKNOWLEDGMENT

The authors acknowledge support from the Department of Energy.

[1] E. H. Lieb, in *Density Functional Methods in Physics*, edited by R. M. Dreizler and J. da Providencia (Plenum, New York, 1985).
[2] B. M. Deb and S. K. Ghosh, in *The Single-Particle Density in Physics and Chemistry*, edited by N. H. March and B. M. Deb (Academic, London, 1987).
[3] E. K. U. Gross and W. Kohn, in *Density Functional Theory of Many-Fermion Systems*, edited by S. B. Trickey (Academic, New York, 1990).
[4] L. D. Landau and E. M. Lifschitz, *Fluid Mechanics* (Pergamon, New York, 1959).
[5] A. C. Eringen, *Mechanics of Nonlinear Continua* (McGraw–Hill, New York, 1962).
[6] E. Madelung, Z. Phys. **40**, 332 (1926).
[7] L. de Broglie, Compt. Rend. **183**, 447 (1926); **184**, 273 (1927); **185**, 380 (1927); **233**, 641 (1951); **234**, 265 (1952); **235**, 557 (1952); **235**, 1345 (1952); **235**, 1435 (1952); **236**, 1453 (1953); **237**, 441 (1953); **239**, 737 (1954); **241**, 345 (1955); **244**, 529 (1957); **264**, 1041 (1967).
[8] D. Bohm, Phys. Rev. **85**, 166 (1952); **85**, 180 (1952); D. Bohm and D. Pines, *ibid.* **85**, 338 (1952); **92**, 609 (1953); D. Bohm and J. Bub, Rev. Mod. Phys. **38**, 453 (1966); D. Bohm, *Ouantum Theory* (Prentice–Hall, New York, 1951), p. 611.
[9] T. Takabayasi, Prog. Theor. Phys. **8**, 143 (1952).
[10] H. E. Wilhelm, Phys. Rev. D **1**, 2278 (1970).
[11] J. H. Weiner and Y. Partom, Phys. Rev. **187**, 1134 (1969).
[12] J. H. Weiner and A. Askar, J. Chem. Phys. **54**, 1108 (1971).
[13] A. Askar and J. H. Weiner, Am. J. Phys. **39**, 1230 (1971).
[14] J. H. Weiner and A. Askar, J. Chem. Phys. **54**, 3534 (1971).
[15] A. Askar and M. Demiralp, J. Chem. Phys. **60**, 2762 (1994).

[16] A. S. Bamzai and B. M. Deb, Rev. Mod. Phys. **53**, 95 (1981); **53**, 593 (1981).
[17] S. K. Ghosh and B. M. Deb, Phys. Rep. **92**, 1 (1982).
[18] B. M. Deb and P. K. Chattaraj, Chem. Phys. Lett. **148**, 550 (1988).
[19] P. K. Chattaraj, S. Rao Koneru, and B. M. Deb, J. Comput. Phys. **72**, 504 (1987).
[20] B. M. Deb and P. K. Chattaraj, in *Solitons; Introduction and Applications*, edited by M. Lakshmanan (Springer, Berlin, 1988).
[21] B. M. Deb and P. K. Chattaraj, Phys. Rev. A **39**, 1696 (1989).
[22] B. M. Deb and S. K. Ghosh, J. Chem. Phys. **77**, 342 (1982).
[23] B. M. Deb and P. K. Chattaraj, Phys. Rev. A **37**, 4030 (1988).
[24] F. M. M. Faisal and U. Schwengelbeck, Phys. Lett. A **207**, 31 (1995); U. Schwengelbeck and F. M. M. Faisal, *ibid.* **199**, 281 (1995).
[25] J. O. Hirschfelder, A. C. Christoph, and W. E. Palke, J. Chem. Phys. **61**, 5435 (1974); J. O. Hirschfelder, C. J. Goebel, and L. W. Bruch, *ibid.* **61**, 5456 (1974); J. O. Hirschfelder and K. T. Tang, *ibid.* **64**, 760 (1976); **65**, 470 (1976).
[26] A. Askar, A. S. Cakmak, and H. Rabitz, J. Chem. Phys. **72**, 5287 (1980).
[27] E. J. Heller, J. Chem. Phys. **62**, 1544 (1995); G. Drolshagen and E. J. Heller, *ibid.* **79**, 2072 (1983); G. Drolshagen and E. J. Heller, *A Wave Packet Approach To Gas–Surface Scattering: Application To Surfaces With Imperfections* (Elsevier, New York, 1983).
[28] E. A. McCullough and R. E. Wyeth, J. Chem. Phys. **51**, 1253 (1969); **54**, 3578 (1961).
[29] W. H. Miller, Adv. Chem. Phys. **25**, 69 (1974); Chem. Phys. Lett. **218**, 189 (1994); L. M. Hubbard and W. H. Miller, J. Chem. Phys. **80**, 5827 (1984).
[30] A. Mostafazadeh, Nucl. Phys. **B509**, 529 (1998).
[31] J. C. Light, I. P. Hamilton, and J. V. Lill, J. Chem. Phys. **82**, 1400 (1985).
[32] R. Kosloff, ''The Fourier Method,'' in *Numerical Grid Methods and their Applications to Schrödinger's Equation*, NATO ASI Series, edited by C. Cerjan (Kluwer Academic, New York, 1993), Vol. 412.
[33] K. C. Kullander, Compt. Phys. Commun. **63** (1991).
[34] J. Von Neumann and R. D. Richtmyer, J. Appl. Phys. **21**, 232 (1950).
[35] W. P. Crowley, ''Free-Lagrange for compressible hydrodynamics in two space dimensions,'' in *The Free-Lagrange Method, Lecture Notes in Physics*, edited by M. J. Frits, W. Crowlen, and H. Trease (Springer, Berlin, 1986).
[36] G. Erlebacher, ''Finite difference operators on unstructured triangular meshes,'' in *The Free-Lagrange Method, Lecture Notes in Physics*, edited by M. J. Fritts, W. P. Crowlen, and H. Trease (Springer, Berlin, 1986), Vol. 238.
[37] D. E. Burton, ''Exact conservation of energy and momentum in staggered-grid hydrodynamics with arbitrary connectivity,'' in *Advances in the Free-Lagrange Method, Lecture Notes in Physics*, edited by H. Trease, M. J. Fritts, and W. P. Crowlen (Sprinser, Berlin, 1991).
[38] R. A. Clark, ''Recent modifications in the HOBO mesh,'' in *Advances in the Free-Lagrange Method, Lecture Notes in Physics*, edited by H. Trease, M. J. Fritts, and W. P. Crowlen (Springer, Berlin, 1992).
[39] K. Miller and R. N. Miller, SIAM (Soc. Ind. Appl. Math.) J. Numer. Anal. **18**, 1019 (1981).
[40] P. J. Boris, A. M. Lansberg, E. S. Oran, and J. H. Gardner, LCPFT-A flux-corrected transport algorithm for solving generalized continuity equations, Naval research Laboratory, Report No. NRL/MR6410-93-7192, 1993; P. J. Boris, F. F. Grinstein, E. S. Oran, and R. L. Kolbe, Fluid Dyn. Res. **10**, 199 (1992).
[41] D. Kroner, *Numerical Schemes for Conservation Laws* (Wiley and Teubner, New York, 1997).
[42] B. K. Dey, A. Askar, and H. A. Rabitz, J. Chem. Phys. (in press).
[43] T.-S. Ho and H. Rabitz, J. Chem. Phys. **104**, 2584 (1996).
[44] T. Hollebeek, T.-S. Ho, and H. Rabitz, J. Chem. Phys. **106**, 7223 (1997).
[45] T.-S. Ho, T. Hollebeek, H. Rabitz, L. B. Harding, and G. C. Schatz, J. Chem. Phys. **105**, 10472 (1996).
[46] G. C. Schatz, A. Papaioannou, L. R. Harding, T. Hollebeek, T.-S. Ho, and H. Rabitz, J. Chem. Phys. **107**, 2340 (1997).
[47] A. Askar and A. Cakmak, J. Chem. Phys. **68**, 2794 (1978).
[48] U. Manthe, H. D. Meyer, and L. S. Cederbaum, J. Chem. Phys. **97**, 3199 (1992).
[49] U. Manthe, H. D. Meyer, and L. S. Cederbaum, J. Chem. Phys. **97**, 9062 (1992).
[50] R. Schinke, *Photodissociation Dynamics* (Cambridge University Press, Cambridge, 1993).
[51] R. Schinke and V. Engel, J. Chem. Phys. **93**, 3252 (1990).
[52] A. Untch, K. Weide, and R. Schinke, J. Chem. Phys. **95**, 6496 (1991).
[53] G. Hirsch and R. J. Buenker, Mol. Phys. **73**, 1085 (1991).
[54] G. G. Balint-Kurti, R. N. R. Dixon, and C. C. Marston, Int. Rev. Phys. Chem. **11**, 317 (1992).
[55] K. C. Kulander, C. Cerjan, and A. E. Orel, J. Chem. Phys. **94**, 2571 (1991).
[56] N. Balakrishnan and N. Sathyamurthy, Chem. Phys. Lett. **240**, 119 (1995).
[57] N. Chakrabarti, V. Balasubramanian, N. Sathyamurthy, and J. W. Gadzuk, Chem. Phys. Lett. **242**, 490 (1995).
[58] See various articles, in *Numerical Grid Methods and their Applications to Schrödinger's Equation*, NATO ASI Series, edited by C. Cerjan (Kluwer Academic, New York, 1993), p. 412.
[59] K. J. Bathe and E. T. Wilson, *Numerical Methods in Finite Elements* (Prentice–Hall, Englewood Cliffs, 1976).
[60] R. H. MacNeal, *Finite elements: Their design and performance* (Dekker, New York, 1994).
[61] A. Askar, ''Finite Elements Method for Quantum Scattering,'' in *Numerical Grid Methods and their Applications to Schrödinger's Equation*, NATO ASI Series, edited by C. Cerjan (Kluwer Academic, New York, 1993), p. 412.
[62] M. J. Fritte and J. P. Boris, J. Comput. Phys. **31**, 173 (1979).